Room-temperature ferromagnetism in transparent Mn-doped $BaSnO_3$ epitaxial films

2014 Appl. Phys. Express 7 033006

(http://iopscience.iop.org/1882-0786/7/3/033006)

Applied Physics Express 7, 033006 (2014)
http://dx.doi.org/10.7567/APEX.7.033006

Room-temperature ferromagnetism in transparent Mn-doped $BaSnO_3$ epitaxial films

Qinzhuang Liu[1*], Yunhua He[1], Hong Li[1], Bing Li[1], Guanyin Gao[2], Lele Fan[3], and Jianming Dai[4]

[1]School of Physics and Electronic Information, Huaibei Normal University, Huaibei 235000, P. R. China
[2]Hefei National Laboratory for Physical Sciences at Microscale, University of Science and Technology of China, Hefei 230029, P. R. China
[3]National Synchrotron Radiation Laboratory, University of Science and Technology of China, Hefei 230029, P. R. China
[4]Institute of Solid State Physics, Chinese Academy of Science, Hefei 230031, P. R. China
E-mail: qzliu@mail.ustc.edu.cn

Received December 19, 2013; accepted February 12, 2014; published online March 6, 2014

Room-temperature ferromagnetism was observed in transparent Mn-doped $BaSnO_3$ (BSMO) films epitaxially grown on $SrTiO_3$ substrates by pulsed laser deposition. X-ray photoelectron spectroscopy and X-ray absorption near-edge structure spectra analysis revealed that Mn^{2+} is the primary Mn ion in the BSMO films. The high saturated magnetization of BSMO films grown at a low oxygen pressure can be attributed to the effective exchange coupling interaction between oxygen vacancies and magnetic Mn ions. Further, the band gap energy of the BSMO films increases from 3.27 to 3.74 eV with decreasing growth oxygen pressure. The results demonstrate that Mn-doped $BaSnO_3$ films may be useful in integrated magneto-optical device applications.

Obtaining room-temperature ferromagnetism (RT-FM) in semiconductor oxides by doping with transition metal (TM) elements has attracted much attention because of potential applications in spintronics. In particular, TM-doped wide band gap oxide semiconductors, such as Co-doped ZnO and Mn- or Co-doped SnO_2 and TiO_2, were extensively investigated in the past decade owing to their wide band gap, high optical transparency, and large magneto-optical response.[1–4] To date, several models have been proposed to explain the origin of the FM observed in semiconductor materials, including double exchange, carrier-mediated exchange, and bound magnetic polarons.[5–7] However, the mechanism responsible for the ferromagnetic interaction is still under debate, though it is generally accepted that structural defects present in the materials may well play an important role in the appearance of ferromagnetic ordering. It is necessary to develop other wide band gap materials that exhibit RT-FM to better understand the origin of the FM. Among the oxide semiconductors, perovskite-structured oxides are an important class of materials that can introduce novel functionalities to electronic devices because of the richness of their excellent electronic, magnetic, optical, and multiferroic properties. Recently, the induction of RT-FM by doping nonmagnetic perovskite-structured materials with a TM, for example, Co- or Fe-doped $SrTiO_3$, Co-doped $BaTiO_3$, and Co-doped $Ba_{0.5}Sr_{0.5}TiO_3$,[8–12] was intensively studied because the addition of spin functionality to the host crystal significantly expands its applications.

Perovskite-structured alkaline earth stannates, with the general formula $RSnO_3$ (R = Ba, Sr, or Ca), have attracted considerable attention in recent years owing to their interesting physical properties and a number of potential applications in the electronics industry. Among $RSnO_3$ compounds, the wide band gap semiconductor $BaSnO_3$ (3.4 eV) has a cubic unit cell and can remain stable even at high temperatures.[13,14] Undoped $BaSnO_3$ has been found to be useful in thermally stable capacitors, humidity sensors, gas sensors, and other applications. Many ions were recently chosen to dope $BaSnO_3$ ceramics to probe their structure, electrical conduction, and dielectric properties.[15–17] La and Sb doping can increase the RT electronic conductivity of $BaSnO_3$ significantly.[18–20] Sr and Pb doping was found to tune the band gap and enhance the photocatalytic activity of $BaSnO_3$.[21–23] Interestingly, Balamurugan et al.[24,25] reported more recently that Mn- and Fe-doped $BaSnO_3$ ceramics exhibit moderate RT-FM. Although $BaSnO_3$ polycrystalline ceramics may have potential applications and were studied in detail, $BaSnO_3$ in thin-film form is much more attractive in terms of basic science and applications. The properties of bulk and thin-film materials, especially dilute magnetic semiconductors, differ greatly. On one hand, the lattice strains induced by the substrate in epitaxial films would modulate the film properties compared to those of bulk materials. On the other hand, oxygen vacancies might easily be generated during various thin-film growth processes owing to the use of vacuum environment, and oxygen vacancies have been suggested to play an important role in the origins of the magnetism.[26] Therefore, it is necessary to investigate the structural and magnetic properties of perovskite-structured TM-ion-doped $BaSnO_3$ films. In this paper, we report transparent 5%-Mn-doped $BaSnO_3$ (BSMO) films grown epitaxially on $SrTiO_3$(001) [STO(001)] substrates by pulsed laser deposition. The structure and properties were characterized in detail, and RT-FM was observed in the BSMO films.

Single-phase ceramic targets of $Ba(Sn_{0.95}Mn_{0.05})O_3$ were synthesized by conventional solid-state reactions using high-purity $BaCO_3$, SnO_2, and MnO_2. Epitaxial BSMO films were deposited on STO(001) single-crystalline substrates by laser ablation using a 248 nm KrF excimer laser. The laser repetition rate was set to 10 Hz, and the laser energy density was maintained at about 1.8 J/cm^2 on the rotating target surface. During deposition, the substrate temperature and oxygen pressure were kept at 780 °C and 1.0×10^{-3} Pa, respectively. For comparison, samples were also grown under an oxygen pressure of 20 Pa on an STO(001) substrate at 780 °C. The film thicknesses were determined to be 630 ± 30 nm by using field emission scanning electron microscopy. The film structures were characterized by X-ray diffraction (XRD) using Cu Kα_1 radiation with $\lambda = 1.5406$ Å (Philips X'pert). X-ray photoelectron spectroscopy (XPS; VG Scientific ESCALAB-250) measurements were made to identify the composition and electronic states of the films using Al Kα X-radiation ($h\nu = 1486.6$ eV, 15 kV, 10 mA). The binding energies of the spectra were internally calibrated using the maximum of the adventitious C 1s signal at 284.6 eV. X-ray absorption near-edge structure (XANES) spectra were recorded under the total electron yield detection mode at the National Synchrotron Radiation Laboratory in Hefei, China. A vibrating sample

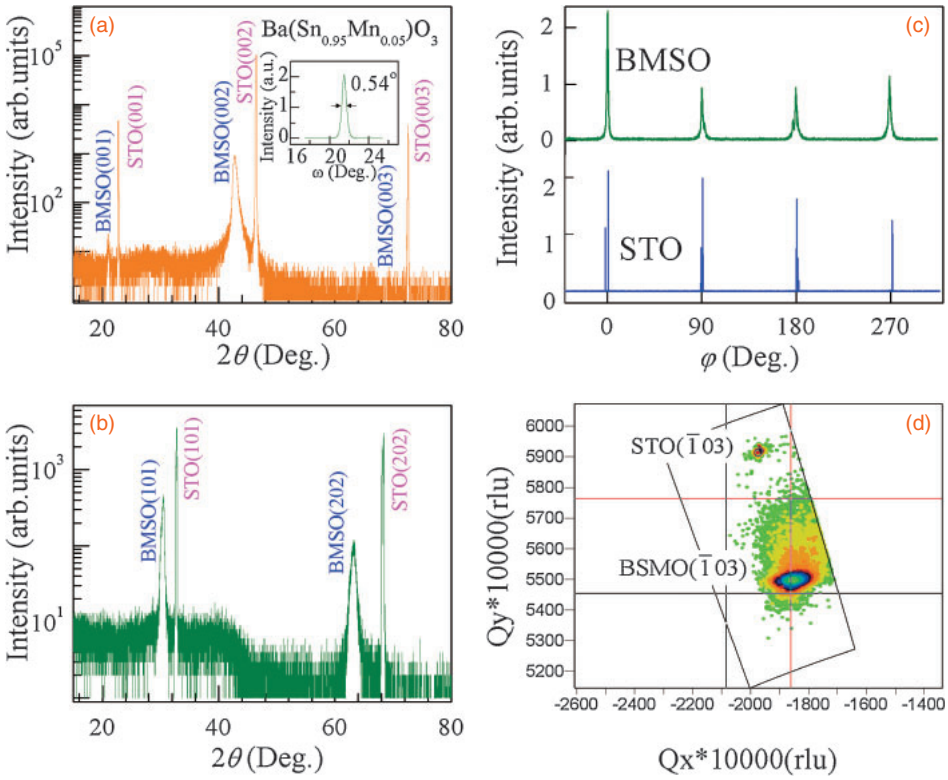

Fig. 1. XRD linear scans of BSMO/STO(001) heterostructures grown in 1×10^{-3} Pa oxygen atmosphere along normal of (a) STO(001) and (b) STO(101) diffraction planes. Inset of (a) shows ω-scan rocking curve of BSMO(002) peak. (c) Φ scans of BSMO(202) and STO(202) reflections. (d) Asymmetric XRD reciprocal space mapping on ($\bar{1}03$) reflections from BSMO/STO(001) heterostructures.

magnetometer (Quantum Design) was used to measure the magnetic properties of the films. The optical transmission spectra were measured with a conventional spectrophotometer (Hitachi U-4100).

Figures 1(a) and 1(b) show the X-ray θ–2θ linear scans of the BSMO/STO(001) heterostructures along the normal of the STO(001) (specular) and STO(101) (off-specular) diffraction planes, respectively. The reflections from the (101) diffraction plane were indexed according to the cubic perovskite structure [Fig. 1(b)]. Only reflections from the (001) planes of the BSMO films and STO substrates were observed in Fig. 1(a). No diffraction peak from impurity phases or randomly oriented grains appeared in the scans, indicating that the films exhibit a preferred orientation along the c-axis. The inset of Fig. 1(a) shows the ω-scan rocking curve (RC) of the BSMO(002) peak. The full width at half-maximum of the RC at the (002) peaks was 0.54°, confirming the high crystallinity of the films. The out-of-plane lattice parameter of the BSMO film was calculated to be 4.2284 ± 0.0017 Å, which is much larger than the value of 4.1176 ± 0.0009 Å obtained for films grown at 20 Pa, whereas the value was 4.1163 Å for pure $BaSnO_3$.[17] This large increase in the lattice parameter was related to the presence of a high concentration of oxygen vacancies in the films, which cause high Coulombic repulsion between the Ba and Sn cations. Because of this electrostatic repulsion, the cations are displaced away from the oxygen vacancies. As a result, the lattice parameter increases, and the unit cell volume expands proportionally.[27] To check the epitaxial properties, Φ scans of the BSMO(202) and STO(202) reflections were performed, as shown in Fig. 1(c). A set of four distinct peaks separated by 90° indicates that the heterostructure achieved parallel epitaxial growth. Figure 1(d) shows the X-ray asymmetric reciprocal space mapping on the ($\bar{1}03$) reflections from the BSMO/STO(001) heterostructure. Q_x and Q_y are coordinates in the reciprocal space, and the in-plane and out-of-plane lattice constants of the film in real space can be determined from the Q_x and Q_y values using $a = -\lambda/2Q_x$ and $c = 3\lambda/2Q_y$.[28] It was found that because of a large lattice mismatch (8.28%) between the film and the substrate, the BSMO films are fully strain-relaxed, and a pseudocubic perovskite structure was formed.

The valence state of Mn ions in BSMO films was characterized by XPS and XANES. Figure 2(a) shows the XPS core-level spectrum of Mn 2p in the BSMO films. The two peaks located at binding energies of 640.1 and 653.2 eV correspond to Mn $2p_{3/2}$ and $2p_{1/2}$ components arising from spin–orbital interaction, respectively. Considering that the $2p_{3/2}$ peaks of Mn^{2+}, Mn^{3+}, and Mn^{4+} ions in oxides are located at binding energies of 640.0–640.6, 641.1–641.7, and 642.7–645.0 eV, respectively, and that of metallic Mn is located at 637.7–639 eV,[29–31] we estimate that the Mn ions in the BSMO films are mainly Mn^{2+}. Because the BSMO films were deposited at a low oxygen pressure and are apt to contain oxygen vacancies, the low valence state of the Mn ions can maintain the charge balance. The low valence state also gives rise to a large average diameter of Mn ions (Mn^{2+}: $R_{ef} = 0.80$ Å, Mn^{3+}: $R_{ef} = 0.58$ Å),[32] which is consistent with the observed lattice expansion.

Although XPS provides information on the valence states of Mn ions, only several nanometers of the surface layer of the BSMO film can be probed. It is necessary to investigate the Mn valence states and local environments over a larger sampling depth. Figure 2(b) shows the measured XANES spectra at the Mn K edge. For comparison, the absorption

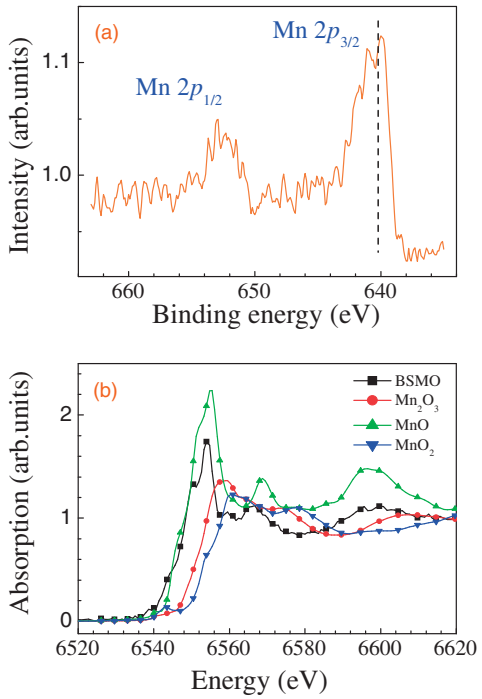

Fig. 2. (a) XPS core level spectrum of Mn 2p peaks in BSMO films grown in 1×10^{-3} Pa oxygen atmosphere. (b) Mn K-edge XANES spectrum of BSMO film deposited at 1.0×10^{-3} Pa, with MnO, Mn_2O_3, and MnO_2 chemical powders as references.

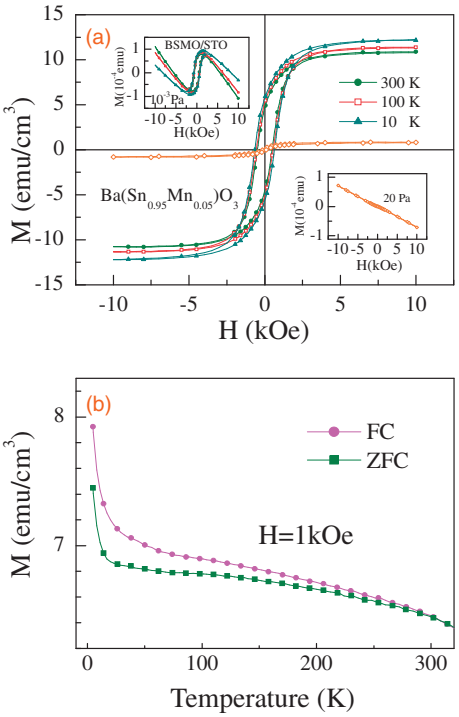

Fig. 3. (a) Magnetization–field loop curves of BSMO films at various temperatures. Insets show original ferromagnetic signal from BSMO/STO heterostructures deposited in 1×10^{-3} and 20 Pa oxygen atmosphere, respectively. (b) Zero-field-cooled and field-cooled magnetization of BSMO films under a magnetic field of 1 kOe as a function of temperature.

spectra of MnO, Mn_2O_3, and MnO_2 chemical powders were also measured. On the energy scale, the onset and shape of the Mn-K absorption spectra for the BSMO films were found to almost match that of MnO, which directly suggests that Mn has an oxidation state of +2. The conclusion regarding the Mn^{2+} valence state is also confirmed by the pre-edge features originating from the p–d hybridization of BSMO films. Titov et al.[33] reported that the Mn charge state in octahedrally or tetrahedrally coordinated Mn compounds can be obtained from the pre-edge spectral features originating in p–d hybridization. A single pre-edge peak indicates Mn^{2+}, whereas a double pre-edge peak indicates Mn^{3+}. In the spectra of the BSMO films, the appearance of a single peak at the Mn pre-edge also support the presence of Mn^{2+}. This qualitative estimate is consistent with the XPS results. The same valence state of Mn^{2+} ions has been reported in many other oxide semiconductor films that exhibit RT-FM.[34–36]

Figure 3(a) shows the magnetic hysteresis loops of the BSMO films at 10, 100, and 300 K, where the magnetic field was applied parallel to the surface plane of the sample. The insets of Fig. 3(a) show the original ferromagnetic signals from BSMO/STO heterostructures prepared at different oxygen pressures. The hysteresis loops were obtained by subtracting the diamagnetic signal from the STO substrates. The BSMO films grown at 1.0×10^{-3} Pa show RT ferromagnetic behavior. With decreasing temperature, the saturated magnetization (M_s) and coercivity field increase from 10.86 emu/cm^3 and 490.2 Oe to 12.25 emu/cm^3 and 650.2 Oe, respectively. Considering the total molar ratio of Mn in the BSMO films, we obtain a value of $M_s = 1.77 \pm 0.10\ \mu_B$/Mn and a remnant magnetization of $0.68 \pm 0.04\ \mu_B$/Mn at 300 K. However, the BSMO films deposited under an oxygen pressure of 20 Pa have a relatively low M_s (0.125 μ_B/Mn), which is associated with the low oxygen vacancy (defect) concentrations of the films. These observations suggest that oxygen vacancies play a significant role in determining the magnetic properties as well as the valence states of Mn ions in BSMO films. Figure 3(b) shows the temperature dependence of the zero-field-cooled (ZFC) and field-cooled (FC) magnetization of the BSMO films measured between 10 and 320 K under a magnetic field of 1 kOe. The FC and ZFC magnetization curves diverge at low temperature, indicating spin-glass behavior of the BSMO films. This can be attributed to a competition between the ferromagnetic and antiferromagnetic interactions.[8] The smooth ZFC curve in the measured temperature range also substantiates the existence of intrinsic RT-FM and the absence of magnetic nanoparticles in the BSMO films. Similar behaviors have been reported in various magnetically doped perovskite-structured films, such as $SrTi_{1-x}Fe_xO_3$, $SrTi_{1-x}Co_xO_3$, and $BaTi_{0.95}Co_{0.05}O_3$ films.[8–11]

The BSMO films grown both at high and low oxygen pressure exhibit highly insulating properties ($\rho \sim 10^7\ \Omega$ cm), indicating that free-carrier-mediated ferromagnetic exchange is not the mechanism operating in BSMO films. Mn metal and Mn-based oxides (MnO, Mn_2O_3, and MnO_2) are either antiferromagnetic or ferromagnetic, with a low Curie temperature of 45 K, confirming that the observed ferromagnetic interactions are the result of the substitution of Mn atoms. The FM in the BSMO films may originate in the exchange interaction between oxygen vacancies and magnetic Mn ions and the formation of magnetic polarons. Trapped electrons couple with local magnetic Mn ions and could generate a large net magnetic moment. Because sufficient oxygen vacancies are present, the coalescence of the magnetic polarons becomes more likely, and the ferromagnetic domain could finally form.

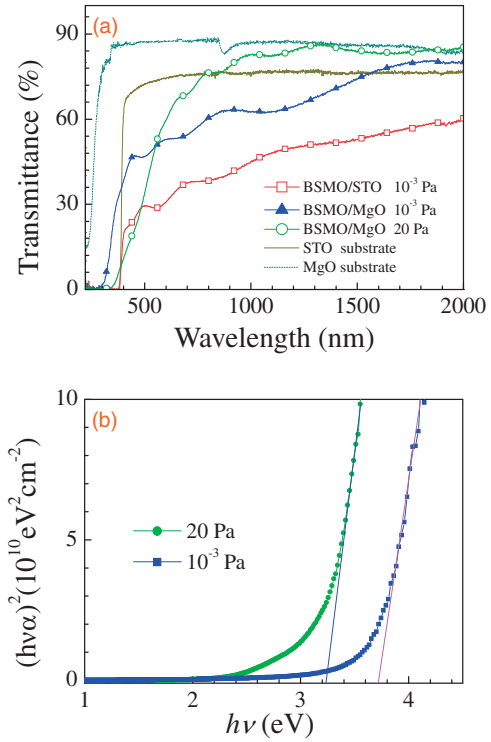

Fig. 4. (a) Optical transmission spectra of BSMO films grown at different oxygen pressures. Optical transmission spectra of bare STO and MgO substrates are shown for comparison. (b) $(h\nu\alpha)^2$ versus $h\nu$ plots of BSMO films deposited on MgO substrate at 1×10^{-3} and 20 Pa oxygen atmosphere, respectively.

Therefore, the magnetism of the BSMO films could be ascribed to the significant contribution of oxygen vacancies that were formed under the oxygen-deficient growth condition.

Because the band gap of the STO substrates (3.2 eV) is smaller than that of the BSMO films, we grew BSMO films on MgO substrates (with a band gap of 7.8 eV) under the same conditions to probe the band gap. For comparison, the transmittances of the bare STO and MgO substrates were also measured, as shown in Fig. 4(a). The films grown at an oxygen pressure of 20 Pa exhibited a good transparency of more than 90% in the visible region, whereas the films deposited at a low oxygen pressure of 1.0×10^{-3} Pa have somewhat low transmittance in the visible region. This may be related to the presence of many oxygen vacancies in the BSMO films. Similar phenomena were also observed in HfO_{2-x} films and Mn-doped SnO_2 films.[34,37)]

The optical direct allowed band gap (E_g) of the BSMO films was determined from the absorption spectra. Figure 4(b) shows plots of $(h\nu\alpha)^2$ against $h\nu$; the values of E_g were estimated to be 3.27 ± 0.06 and 3.74 ± 0.04 eV for the BSMO films grown at high and low oxygen pressures, respectively, by extrapolating the linear portion against the photon energy. The band gap increase of the BSMO films grown at the low oxygen pressure can be ascribed to the expansion of the unit cell volume.[38)]

Acknowledgments This work was supported by the Chinese Natural Science Foundation (Nos. 11004071, 11374304), Natural Science Foundation of Anhui Province (1408085QA19), and Huaibei Scientific Talent Development Scheme (No. 20130304).

1) J. L. MacManus-Driscoll, N. Khare, Y. Liu, and M. E. Vickers, Adv. Mater. **19**, 2925 (2007).
2) H.-S. Kim, L. Bi, G. F. Dionne, C. A. Ross, and H.-J. Paik, Phys. Rev. B **77**, 214436 (2008).
3) K. G. Roberts, M. Varela, S. Rashkeev, S. T. Pantelides, S. J. Pennycook, and K. M. Krishnan, Phys. Rev. B **78**, 014409 (2008).
4) S. Y. Park, P. J. Kim, Y. P. Lee, S. W. Shin, T. H. Kim, J.-H. Kang, and J. Y. Rhee, Adv. Mater. **19**, 3496 (2007).
5) J. M. D. Coey, M. Venkatesan, and C. B. Fitzgerald, Nat. Mater. **4**, 173 (2005).
6) M. H. F. Sluiter, Y. Kawazoe, P. Sharma, A. Inoue, A. R. Raju, C. Rout, and U. V. Waghmare, Phys. Rev. Lett. **94**, 187204 (2005).
7) M. S. Park, S. K. Kwon, and B. I. Min, Phys. Rev. B **65**, 161201 (2002).
8) H.-S. Kim, L. Bi, D. H. Kim, D.-J. Yang, Y. J. Choi, J. W. Lee, J. K. Kang, Y. C. Park, G. F. Dionne, and C. A. Ross, J. Mater. Chem. **21**, 10364 (2011).
9) H.-S. Kim, L. Bi, G. F. Dionne, and C. A. Ross, Appl. Phys. Lett. **93**, 092506 (2008).
10) Y.-H. Lin, S. Zhang, C. Deng, Y. Zhang, X. Wang, and C.-W. Nan, Appl. Phys. Lett. **92**, 112501 (2008).
11) A. B. Posadas, C. Mitra, C. Lin, A. Dhamdhere, D. J. Smith, M. Tsoi, and A. A. Demkov, Phys. Rev. B **87**, 144422 (2013).
12) L. B. Luo, Y. G. Zhao, H. F. Tian, J. J. Yang, H. Y. Zhang, J. Q. Li, J. J. Ding, B. He, S. Q. Wei, and C. Gao, Appl. Phys. Lett. **92**, 232507 (2008).
13) J. Cerdà, J. Arbiol, R. Diaz, G. Dezanneau, and J. R. Morante, Mater. Lett. **56**, 131 (2002).
14) Q. Liu, J. Liu, B. Li, H. Li, G. Zhu, K. Dai, Z. Liu, P. Zhang, and J. Dai, Appl. Phys. Lett. **101**, 241901 (2012).
15) Y. Shimizu, Y. Fukuyama, T. Narikiyo, H. Arai, and T. Seiyama, Chem. Lett. **14**, 377 (1985).
16) B. Hadjarab, A. Bouguelia, A. Benchettara, and A. Trari, J. Alloys Compd. **461**, 360 (2008).
17) S. Upadhyay, O. Parkash, and D. Kumar, J. Electroceram. **18**, 45 (2007).
18) H. J. Kim, U. Kim, H. M. Kim, T. H. Kim, H. S. Mun, B.-G. Jeon, K. T. Hong, W.-J. Lee, C. Ju, K. H. Kim, and K. Char, Appl. Phys. Express **5**, 061102 (2012).
19) S. Upadhyay, O. Parkash, and D. Kumar, J. Phys. D **37**, 1483 (2004).
20) W. Lu, S. Jiang, D. Zhou, and S. Gong, Sens. Actuators **80**, 35 (2000).
21) H. Mizoguchi, P. M. Woodward, C.-H. Park, and D. A. Keszler, J. Am. Chem. Soc. **126**, 9796 (2004).
22) Y. Yuan, J. Lv, X. Jiang, Z. Li, T. Yu, Z. Zou, and J. Ye, Appl. Phys. Lett. **91**, 094107 (2007).
23) P. H. Borse, U. A. Joshi, S. M. Ji, J. S. Jang, J. S. Lee, E. D. Jeong, and H. G. Kim, Appl. Phys. Lett. **90**, 034103 (2007).
24) K. Balamurugan, N. Harish Kumar, B. Ramachandran, M. S. Ramachandra Rao, J. Arout Chelvane, and P. N. Santhosh, Solid State Commun. **149**, 884 (2009).
25) K. Balamurugan, N. Harish Kumar, J. Arout Chelvane, and P. N. Santhosh, J. Alloys Compd. **472**, 9 (2009).
26) C. D. Pemmaraju, R. Hanafin, T. Archer, H. B. Braun, and S. Sanvito, Phys. Rev. B **78**, 054428 (2008).
27) R. Perez-Casero, J. Perrière, A. Gutierrez-Llorente, D. Defourneau, E. Millon, W. Seiler, and L. Soriano, Phys. Rev. B **75**, 165317 (2007).
28) F. Chen, H. F. Wang, Q. Z. Liu, W. Wu, and X.-G. Li, Appl. Phys. Lett. **90**, 082904 (2007).
29) C. J. Cong and K. L. Zhang, Phys. Status Solidi B **243**, 2764 (2006).
30) S. A. Chambers and Y. Liang, Surf. Sci. **420**, 123 (1999).
31) S. R. S. Kumar, M. N. Hedhili, H. N. Alshareef, and S. Kasiviswanathan, Appl. Phys. Lett. **97**, 111909 (2010).
32) I. V. Ol'khovik, E. D. Politova, A. V. Mitin, S. G. Prutchenko, and M. V. Fedotova, Inorg. Mater. **30**, 380 (1994).
33) A. Titov, X. Biquard, D. Halley, S. Kuroda, E. Bellet-Amalric, H. Mariette, J. Cibert, A. E. Merad, G. Merad, M. B. Kanoun, E. Kulatov, and Y. A. Uspenskii, Phys. Rev. B **72**, 115209 (2005).
34) S. J. Liu, C. Y. Liu, J. Y. Juang, and H. W. Fang, J. Appl. Phys. **105**, 013928 (2009).
35) X. Y. Li, S. X. Wu, L. M. Xu, C. T. Li, Y. J. Liu, X. J. Xing, and S. W. Li, Mater. Sci. Eng. B **156**, 90 (2009).
36) Y. Liu, S. Yang, Y. Zhang, and D. Bao, J. Magn. Magn. Mater. **321**, 3406 (2009).
37) E. Hildebrandt, J. Kurian, M. M. Müller, T. Schroeder, H.-J. Kleebe, and L. Alff, Appl. Phys. Lett. **99**, 112902 (2011).
38) S. Lee, W. H. Woodford, and C. A. Randall, Appl. Phys. Lett. **92**, 201909 (2008).